ChemComm

COMMUNICATION

View Article Online
View Journal | View Issue

Check for updates

Cite this: *Chem. Commun.*, 2023, 59, 13771

Received 26th July 2023,
Accepted 23rd October 2023

DOI: 10.1039/d3cc03594h

rsc.li/chemcomm

Open Access Article. Published on 24 October 2023. Downloaded on 2/7/2026 6:14:33 PM.
This article is licensed under a Creative Commons Attribution 3.0 Unported Licence.

Facile synthesis of wide bandgap ZrS_2 colloidal quantum dots for solution processed solar-blind UV photodetectors†

Zan Wang, [abc] Yunjiao Gu, [bcd] Fenghua Liu [bcd] and Weiping Wu *[bcd]

We present a facile one-pot method for the successful synthesis of heavy metal-free ZrS_2 colloidal quantum dots (QDs) with a wide bandgap. To achieve this, we employed 1-dodecanethiol (DT) as a sulfur precursor, enabling the controlled release of H_2S *in situ* during the reaction at temperatures exceeding 195 °C. This approach facilitated the synthesis of small-sized ZrS_2 QDs with precise control.

New blue quantum dot technology has the potential to enhance the energy efficiency of displays, light-emitting devices, and solar-blind UV photodetector devices. Therefore, the development of novel blue quantum dot materials becomes pivotal. Recently, there has been considerable interest in two-dimensional (2D) layered transition-metal dichalcogenides (TMDs) as a promising class of nanomaterials for various important applications, owing to their exceptional properties.[1–4] As new nanomaterials, TMD quantum dots (QDs) display distinctive optical and electronic properties that surpass those of single or few-layer TMD nanosheets. This can be attributed to stronger edge effects and quantum confinement.[5–8]

ZrS_2 is an n-type indirect bandgap semiconductor with a typical layered sandwich structure and exhibits superior stability, excellent electrical properties and a larger bandgap of 1.7 eV.[9–11] Recently, ZrS_2 has been theoretically predicted to have acoustic phonon limited charge carrier mobility ($\sim$1247 $cm^2\ V^{-1}\ s^{-1}$) and high current density (800 $\mu A\ \mu m^{-1}$).[12,13] 2D layered ZrS_2 has been studied for various applications,[14–17] whereas ZrS_2 QDs have rarely been studied. The synthesis of the ZrS_2 QDs poses significant challenges primarily due to the absence of methods for achieving the small size and high crystallinity of the ZrS_2 QDs. Previous studies on ZrS_2 nanostructures have been limited to relatively large sized ZrS_2 nanocrystals, which may be derived from the highly active precursor S element. For example, Jang *et al.* reported a hot-injection route by injecting CS_2 into a mixture of oleylamine and $ZrCl_4$ to synthesize ultrathin ZrS_2 nanodiscs and their lateral size can be tuned from 20 to 60 nm.[18] Recently, Paul *et al.* have employed both heat up and hot injection methods to fabricate colloidal ZrS_2 nanocrystals, and the average sizes of the particles are 15 nm and 41 nm, respectively.[19] Despite the recent progress in the synthesis of the ZrS_2 nanocrystals, it is still a challenge to prepare the ZrS_2 QDs (less than 10 nm in size), especially through colloidal solution-based approaches. Herein, for the first time, we developed a facile colloidal solution-based synthetic method for the preparation of heavy metal-free, small blue ZrS_2 QDs. 1-Dodecanethiol (DT) was chosen as a sulfur precursor to slowly and continuously release the influx of the chalcogen source (*e.g.*, H_2S) *in situ* at a high temperature of 225 °C by reacting with $ZrCl_4$ in oleylamine. The reaction was continued for 1.5 h to generate small sized ZrS_2 QDs (Fig. 1a).

TEM was performed to analyze the morphology and size of the as-synthesized ZrS_2 QDs. The TEM image of the ZrS_2 QDs is shown in Fig. 1b. It can be observed that the ZrS_2 QDs were monodisperse and uniform. Fig. 1c shows the diameter distribution of the ZrS_2 QDs (Fig. 1b), with an average size of 4.93 ± 0.83 nm. The HRTEM image revealed that the ZrS_2 QDs are single-crystalline structures with parallel and ordered lattice fringes and the lattice distances of the particles are 0.32 nm and 0.18 nm, which are assigned to the (100) and (110) planes (Fig. 1d, e). The corresponding FFT pattern is consistent with the HRTEM results and revealed the hexagonal phase lattice structure of the ZrS_2 QDs (Fig. 1f). In addition, the mapping of the elements and merging confirmed that the nanoparticles were composed of Zr and S elements characterized by HAADF-STEM (Fig. 1g).

XRD was used to analyze the crystal structure of the as-synthesized ZrS_2 QDs. As seen in Fig. 2a, the sample exhibits broad and diffuse diffraction peaks, and the major diffraction

[a] *Department of Optics and Optical Engineering, University of Science and Technology of China, Hefei, Anhui, 230026, China*
[b] *Laboratory of Thin Film Optics, Shanghai Institute of Optics and Fine Mechanics, Chinese Academy of Sciences, Shanghai, 201800, China. E-mail: wuwp@siom.ac.cn*
[c] *State Key Laboratory of High Field Laser Physics, Shanghai Institute of Optics and Fine Mechanics, Chinese Academy of Sciences, Shanghai, 201800, China*
[d] *University of Chinese Academy of Sciences, Beijing, 100049, China*

† Electronic supplementary information (ESI) available. See DOI: https://doi.org/10.1039/d3cc03594h

Open Access Article. Published on 24 October 2023. Downloaded on 2/7/2026 6:14:33 PM.
This article is licensed under a Creative Commons Attribution 3.0 Unported Licence.

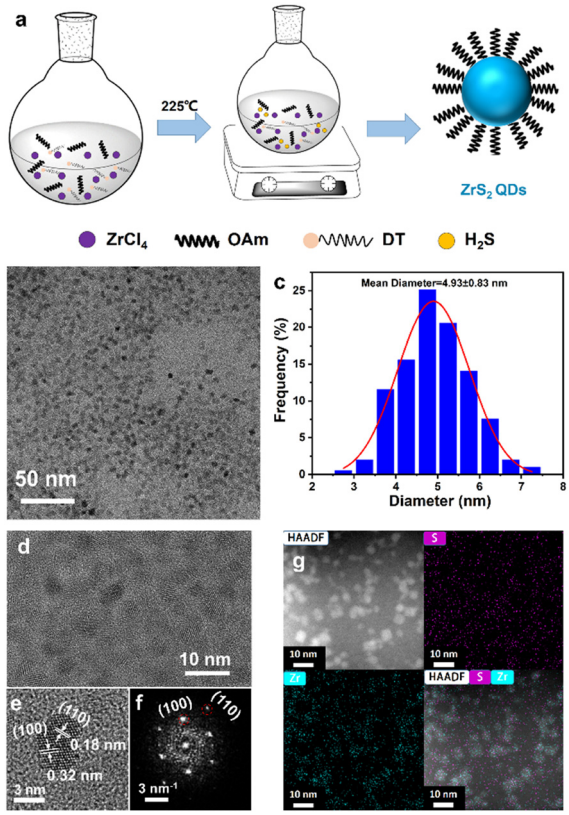

Fig. 1 (a) Schematic representation of the synthesis of ZrS_2 QDs. (b) Low-magnification TEM image and (c) the size distribution of the ZrS_2 QDs. (d) Enlarged TEM image of the ZrS_2 QDs. (e) HRTEM images of the ZrS_2 QDs with different lattice fringes and (f) the corresponding size distribution obtained by FFT. (g) HAADF-STEM images and the corresponding EDS mappings of the ZrS_2 QDs.

peaks at 2θ = 32.2°, 52.4° and 60.5° correspond to the (101), (111) and (201) lattice planes respectively, which can be assigned to the hexagonal phase with $P3m1$ ZrS_2 (JCPDS no. 11-0679) and is in good agreement with the results of HRTEM. The structure of the ZrS_2 QDs was further established by Raman spectra using a laser source operating at a wavelength of 532 nm, as shown in Fig. 2b, exhibiting the feature peaks of bulk zirconium disulfide crystals. The Raman spectra of the ZrS_2 QDs were dominated by two rather broad, symmetric peaks at 320 and 244 cm^{-1}. The stronger peak at 320 cm^{-1} can be attributed to the Zr–S bonds showing vertical out-of-plane vibration, corresponding to the A_{1g} mode. In addition, a weaker non-degenerate in-of-plane vibrational E_g mode was observed at 244 cm^{-1} along with weak phonon modes at approximately 115 and 195 cm^{-1} in agreement with literature.[20,21] In contrast to bulk ZrS_2,[22–24] both the dominant A_{1g} and weak E_g modes of the ZrS_2 QDs are slightly blue-shifted, which can be explained by small lateral dimensions and reduction in the number of layers. The blue-shift phenomenon is similar to the mode change observed for other TMD quantum dots.[25–28]

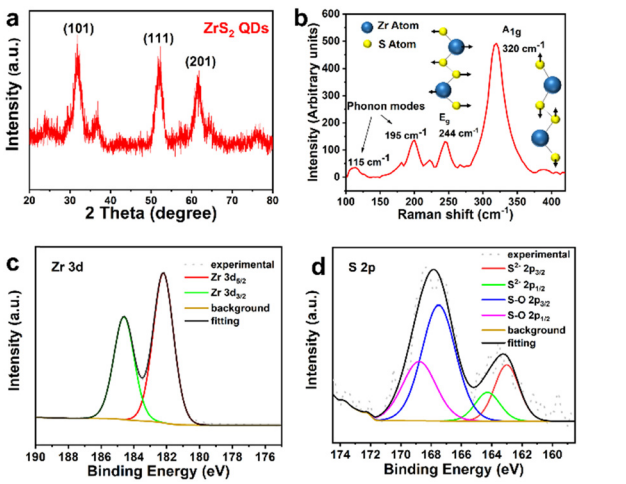

Fig. 2 (a) Powder XRD patterns of ZrS_2 QDs. (b) The Raman spectrum of the ZrS_2 QDs on the Si substrate with schematics of E_g and A_{1g} Raman vibrational modes. High-resolution XPS of (c) Zr 3d and (d) S 2p regions of ZrS_2 QDs.

XPS was used to characterize the chemical compositions and the binding energies of the bonded elements of the ZrS_2 QDs. The survey spectrum indicates that no obvious impurity is observed in the sample, which is consistent with EDS mapping results (Fig. S1, ESI†). In Fig. 2c, the high-resolution Zr 3d region spectra of the ZrS_2 QDs clearly show that the two peaks of Zr $3d_{5/2}$ and Zr $3d_{3/2}$ correspond to the binding energies of 182.3 eV and 184.6 eV, respectively, indicating the oxidation state of Zr^{4+}.[17,29] In contrast, the high-resolution S 2p region spectra were analyzed to elucidate the nature of S element. Fig. 2d shows that the S 2p peaks can be fitted with two doublets of S $2p_{3/2}$ energy states and both of them are accompanied by $2p_{1/2}$ peaks (the binding energy is higher at about 1.2 eV than that of the corresponding $2p_{3/2}$ peak). One doublet appeared at around 163.1 eV, corresponding to intrinsic ZrS_2, and the other peak in the high energy region (at around 167.6 eV) is indicative of sulfate ions, which may be caused by hydration and surface oxidation when the ZrS_2 QDs are exposed to air.[26,30]

The optical properties of the ZrS_2 QDs were investigated by UV-Vis absorption and PL spectroscopy techniques (Fig. 3). The ZrS_2 QDs were dispersed in the cyclohexane solvent and appeared as a claybank colloidal solution under natural light (left insert in Fig. 3a) and the colloidal solution can remain stable for several months at room temperature in air, which was verified by the obvious Tyndall effect (the right inset in Fig. 3a). The absorption spectrum of the ZrS_2 QDs solution is shown in Fig. 3a, which displays a strong absorption in the ultraviolet region with an absorption peak located at around 270 nm and a broad absorption tail in blue and green regions. The bandgap energy of the ZrS_2 QDs is around 3.32 eV calculated by fitting the Tauc plot.[31] The calculated bandgap energy of the ZrS_2 QDs is much higher than that of bulk ZrS_2 crystals (1.7 eV),[32] which can be attributed to the significant quantum confined effects.[33] As for the PL properties of ZrS_2 QDs, the as-obtained ZrS_2 QD solution shows strong luminescence under 365 nm excitation (inset of Fig. 3b). Furthermore, Fig. 3c shows the photoluminescence (PL) spectra of the ZrS_2 QD solution at various

 This journal is © The Royal Society of Chemistry 2023

Open Access Article. Published on 24 October 2023. Downloaded on 2/7/2026 6:14:33 PM.
This article is licensed under a Creative Commons Attribution 3.0 Unported Licence.

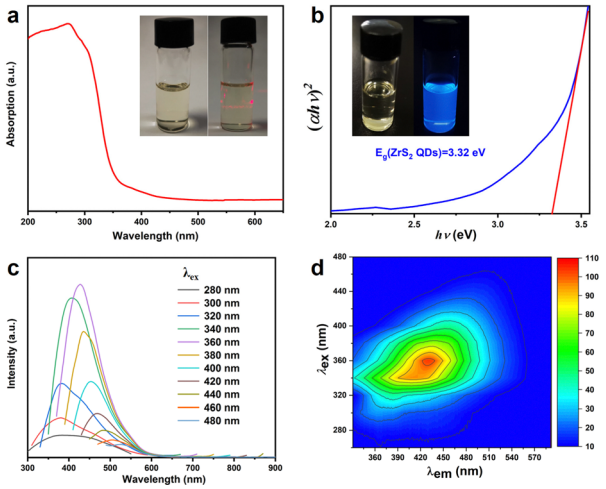

Fig. 3 (a) UV/Vis absorption spectrum of ZrS_2 QDs in cyclohexane solvent. Inset: Photos of the ZrS_2 QD suspension (left) and the Tyndall effect of the ZrS_2 QD suspension (right). (b) Tauc plot for estimating the E_g of the ZrS_2 QDs. Inset: Photographs of the ZrS_2 QDs under sunlight (left) and 365 nm UV light excitation (right). (c) Photoluminescence spectra of the ZrS_2 QDs at different excitation wavelengths. (d) The EEM fluorescence spectra of the ZrS_2 QDs.

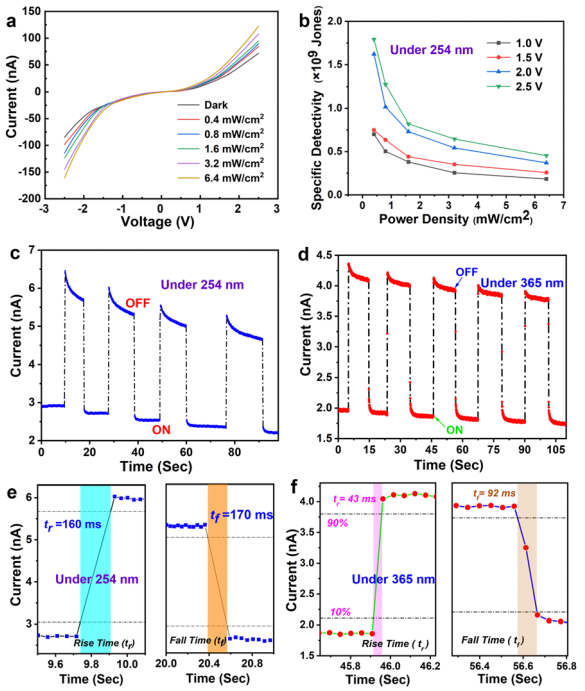

Fig. 4 (a) The *I*–*V* characteristics of the fabricated ZrS_2 QD-based PD in the dark and under 254 nm UV light at different power densities. (b) The specific detectivity of the ZrS_2 QD-based PD was described as the dependence of power density at various applied bias voltages. Time response of the ZrS_2 QD-based PD at 1 V under (c) 254 nm and (d) 365 nm UV illumination at a power density of 6.4 mW cm^{-2}. The *I*–*t* curve for determining the rise and decay times of the ZrS_2 QD-based PD under (e) 254 nm and (f) 365 nm UV illumination.

excitation wavelengths ranging from 280 nm to 480 nm and an excitation-dependent PL behavior is observed for the ZrS_2 QDs. In order to analyze the relationship between excitation and emission clearly, excitation–emission matrix (EEM) fluorescence spectra are plotted in Fig. 3d. The PL intensity of the ZrS_2 QDs increases with increasing excitation wavelength, reaches a maximum at 435 nm at an excitation wavelength of 360 nm, and then decreases. However, it is observed that the PL peaks were redshifted from 360 nm to 540 nm and the PL intensity exhibits a Gaussian distribution as the excitation wavelength changes from 280 nm to 480 nm, respectively. For high-energy excitation at 280–320 nm, the ZrS_2 QDs show a broad excitation-independent PL band behavior. At excitation wavelengths of 340–480 nm (low-energy), the PL peak shows an obvious red-shift with the increase of the excitation wavelength. A similar excitation-dependent PL phenomenon has also been observed for other TMD QDs.[34–37] In such systems, the most comprehensively accepted reason for the excitation-dependent PL phenomenon can be attributed to the size effect (also known as the quantum confinement effect)[38,39] and/or to edge states[40,41] and surface traps.[30,36]

As a proof-of-concept application, the ZrS_2 QDs were used as the active layer for ultraviolet and solar-blind photodetector (PD) devices with the structure of Au/ZrS_2 QDs/Au. The photoelectric properties of the ZrS_2 QD-based PD were then investigated (Fig. 4). The current–voltage (*I*–*V*) characteristic plot shows that the applied voltage ranges from −2.5 V to 2.5 V under dark and under 254 nm (Fig. 4a) and 365 nm (Fig. S3, ESI†) UV illumination at various light densities. The ZrS_2 QD-based PD exhibits obvious photoresponse performance and nonlinear *I*–*V* characteristics, revealing that there may be a small barrier height at the metal–semiconductor (Au-ZrS_2 QDs) junction.[42] Therefore, the contact between Au and ZrS_2 QDs is Schottky rather than Ohmic. In Fig. 4b, the specific detectivity of ZrS_2 QD-based PD was described as the dependence of power density at various applied bias voltages under 254 nm UV illumination, and the specific detectivity decreases with the increase of power density and decrease of the applied bias voltage. This can be attributed to two reasons: on the one hand, the probability of carrier recombination increases when high illumination intensity is applied; on the other hand, the high applied bias voltage helps the carriers to transfer to the electrode.[43] The specific detectivities of the PD were 1.8×10^9, 1.6×10^9, 0.75×10^9, and 0.7×10^9 Jones, corresponding to a power density of 0.4 mW/cm^2 at applied bias voltages from 2.5 to 1 V, respectively. In addition, the specific detectivity of the PD also shows the same trend under 365 nm UV illumination.

Fig. 4c and d show the optical switching of the PD for five consecutive cycles at 1 V bias voltage under 254 nm and 365 nm UV illumination with a power density of 6.4 mW cm^{-2}, revealing the stability and repeatability of the PD. It is worth noting that the photocurrent of the PD decreases with time under 254 nm and 365 nm UV illumination, which is associated with the fact that the photo-generated carriers easily recombine in the defect state, resulting in the decrease of the photocurrent.[44] Fig. 4e shows that the rise time was 160 ms and the fall time was 170 ms under 254 nm illumination. Besides, Fig. 4f shows

Open Access Article. Published on 24 October 2023. Downloaded on 2/7/2026 6:14:33 PM.
This article is licensed under a Creative Commons Attribution 3.0 Unported Licence.

that the rise time was 43 ms and the fall time was 92 ms under 365 nm illumination, indicating the potential application of the ZrS_2 QD-based PD as a highly sensitive optical switch.

In summary, a facile one-pot method was used to successfully synthesize wide bandgap ZrS_2 quantum dots (QDs) without the use of heavy metals. The sulfur precursor 1-dodecanethiol (DT) was selected to gradually release the chalcogen source (*e.g.*, H_2S) at high temperatures, enabling the synthesis of small-sized ZrS_2 QDs. The resulting ZrS_2 QDs, with an average size of 4.93 ± 0.83 nm, possess high crystallinity and demonstrate excellent dispersion and stability in the solvent. Additionally, the ZrS_2 QDs exhibit a wide bandgap of 3.32 eV and photoluminescence behavior that depends on the excitation wavelength. As a proof-of-concept application, a solar-blind UV photodetector was fabricated using Au/ZrS_2 QDs/Au on a glass substrate. The photodetector shows a low dark current (2 nA), high specific detectivity (1.8×10^9 Jones), and fast photoresponse with rise and fall times of 43 and 92 ms, respectively. These heavy metal-free, printable ZrS_2 QDs possess remarkable optoelectronic properties and will have many important potential applications.

This work was supported by the National Natural Science Foundation of China (52273242, 22202231), the National Key R&D Program of China (2021YFB2800703, 2021YFB2800701) and the Chinese Academy of Sciences.

Conflicts of interest

There are no conflicts to declare.

Notes and references

1 Y. Li, H. L. Chen, Y. X. Guo, K. K. Wang, Y. Zhang, P. L. Lan, J. H. Guo, W. Zhang, H. Q. Zhong, Z. Y. Guo, Z. F. Zhuang and Z. M. Liu, *Photonics Res.*, 2021, **9**, 1039–1047.
2 A. Di Bartolomeo, A. Kumar, O. Durante, A. Sessa, E. Faella, L. Viscardi, K. Intonti, F. Giubileo, N. Martucciello, P. Romano, S. Sleziona and M. Schleberger, *Mater. Today Nano*, 2023, **24**, 100382.
3 C. Patil, C. B. Dong, H. Wang, B. M. Nouri, S. Krylyuk, H. R. Zhang, A. V. Davydov, H. Dalir and V. J. Sorger, *Photonics Res.*, 2022, **10**, A97–A105.
4 C. L. Liang, E. Z. Wang, X. Li, J. Wang, Y. J. Liu, B. Y. Chen, H. X. Chen, Y. Liu and X. F. Peng, *Chin. Opt. Lett.*, 2022, **20**, 021901.
5 X. G. Ding, F. Peng, J. Zhou, W. B. Gong, G. Slaven, K. P. Loh, C. T. Lim and D. T. Leong, *Nat. Commun.*, 2019, **10**, 41.
6 R. A. Neville and B. L. Evans, *Phys. Status Solidi B*, 1976, **73**, 597–606.
7 W. H. Dai, H. F. Dong, B. Fugetsu, Y. Cao, H. T. Lu, X. L. Ma and X. J. Zhang, *Small*, 2015, **11**, 4158–4164.
8 S. Y. Cao, L. P. Hou, Q. F. Wang, C. Y. Li, W. X. Yu, X. T. Gan, K. H. Liu, M. Premaratne, F. J. Xiao and J. L. Zhao, *Photonics Res.*, 2021, **9**, 501–506.
9 Y. Tian, Y. Cheng, J. D. Huang, S. Y. Zhang, H. Dong, G. K. Wang, J. R. Chen, J. L. Wu, Z. G. Yin and X. W. Zhang, *Nano Res.*, 2022, **15**, 6628–6635.
10 M. Moustafa, T. Zandt, C. Janowitz and R. Manzke, *Phys. Rev. B: Condens. Matter Mater. Phys.*, 2009, **80**, 035206.
11 T. Zhai, L. Li, X. Wang, X. S. Fang, Y. Bando and D. Golberg, *Adv. Funct. Mater.*, 2010, **20**, 4233–4248.
12 W. X. Zhang, Z. S. Huang, W. L. Zhang and Y. R. Li, *Nano Res.*, 2014, **7**, 1731–1737.
13 G. Fiori, F. Bonaccorso, G. Iannaccone, T. Palacios, D. Neumaier, A. Seabaugh, S. K. Banerjee and L. Colombo, *Nat. Nanotechnol.*, 2014, **9**, 768–779.
14 Z. Y. Zeng, Z. Y. Yin, X. Huang, H. Li, Q. Y. He, G. Lu, F. Boey and H. Zhang, *Angew. Chem., Int. Ed.*, 2011, **50**, 11093–11097.
15 L. Li, X. S. Fang, T. Y. Zhai, M. Y. Liao, U. K. Gautam, X. C. Wu, Y. Koide, Y. Bando and D. Golberg, *Adv. Mater.*, 2010, **22**, 4151–4156.
16 X. R. Zhang, Z. S. Meng, D. W. Rao, Y. H. Wang, Q. Shi, Y. Z. Liu, H. P. Wu, K. M. Deng, H. Y. Liu and R. F. Lu, *Energy Environ. Sci.*, 2016, **9**, 841–849.
17 R. J. Toh, Z. Sofer and M. Pumera, *J. Mater. Chem. A*, 2016, **4**, 18322–18334.
18 J. T. Jang, S. Jeong, J. W. Seo, M. C. Kim, E. Sim, Y. Oh, S. Nam, B. Park and J. Cheon, *J. Am. Chem. Soc.*, 2011, **133**, 7636–7639.
19 P. Fadojutimi, Z. Tetana, J. Moma, N. Moloto and S. Gqoba, *ChemistrySelect*, 2022, **7**, e202202293.
20 A. M. Stacy and D. T. Hodul, *J. Phys. Chem. Solids*, 1985, **46**, 405–409.
21 M. Mattinen, G. Popov, M. Vehkamaki, P. J. King, K. Mizohata, P. Jalkanen, J. Raisanen, M. Leskela and M. Ritala, *Chem. Mater.*, 2019, **31**, 5713–5724.
22 S. Manas-Valero, V. Garcia-Lopez, A. Cantarero and M. Galbiati, *Appl. Sci.*, 2016, **6**, 264.
23 N. Glebko, I. Aleksandrova, G. C. Tewari, T. S. Tripathi, M. Karppinen and A. J. Karttunen, *J. Phys. Chem. C*, 2018, **122**, 26835–26844.
24 S. M. Oliver, J. J. Fox, A. Hashemi, A. Singh, R. L. Cavalero, S. Yee, D. W. Snyder, R. Jaramillo, H. P. Komsa and P. M. Vora, *J. Mater. Chem. C*, 2020, **8**, 5732–5743.
25 V. Stengl and J. Henych, *Nanoscale*, 2013, **5**, 3387–3394.
26 D. Dinda, M. E. Ahmed, S. Mandal, B. Mondal and S. K. Saha, *J. Mater. Chem. A*, 2016, **4**, 15486–15493.
27 X. Zhang, H. M. Xie, Z. D. Liu, C. L. Tan, Z. M. Luo, H. Li, J. D. Lin, L. Q. Sun, W. Chen, Z. C. Xu, L. H. Xie, W. Huang and H. Zhang, *Angew. Chem., Int. Ed.*, 2015, **54**, 3653–3657.
28 C. Wang, J. Gao, J. G. Zhao, D. J. Yan and X. D. Zhu, *Small*, 2020, **16**, 1907091.
29 M. Zhang, Y. Zhu, X. Wang, Q. Feng, S. Qiao, W. Wen, Y. Chen, M. Cui, J. Zhang, C. Cai and L. Xie, *J. Am. Chem. Soc.*, 2015, **137**, 7051–7054.
30 B. Li, L. Jiang, X. Li, P. Ran, P. Zuo, A. D. Wang, L. T. Qu, Y. Zhao, Z. H. Cheng and Y. F. Lu, *Sci. Rep.*, 2017, **7**, 11182.
31 P. Makula, M. Pacia and W. Macyk, *J. Phys. Chem. Lett.*, 2018, **9**, 6814–6817.
32 E. Martino, D. Santos-Cottin, F. Le Mardele, K. Semeniuk, M. Pizzochero, K. Cernevics, B. Baptiste, L. Delbes, S. Klotz, F. Capitani, H. Berger, O. V. Yazyev and A. Akrap, *ACS Mater. Lett.*, 2020, **2**, 1115–1120.
33 T. Z. Wu, Y. Lin, Y. M. Huang, M. Liu, K. J. Singh, W. S. Lin, T. W. Lu, X. Zheng, J. Y. Zhou, H. C. Kuo and Z. Chen, *Photonics Res.*, 2021, **9**, 2132–2143.
34 A. S. Sarkar, A. Kumari, Anchala, N. Nakka, R. Ray, E. Stratakis and S. K. Pal, *Appl. Phys. Lett.*, 2021, **119**, 241902.
35 W. Gu, Y. H. Yan, C. L. Zhang, C. P. Ding and Y. Z. Xian, *ACS Appl. Mater. Interfaces*, 2016, **8**, 11272–11279.
36 D. Gopalakrishnan, D. Damien, B. Li, H. Gullappalli, V. K. Pillai, P. M. Ajayan and M. M. Shaijumon, *Chem. Commun.*, 2015, **51**, 6293–6296.
37 R. K. Behera, L. Mishra, A. Panigrahi, P. K. Sahoo and M. K. Sarangi, *ACS Appl. Mater. Interfaces*, 2022, **14**, 5750–5761.
38 D. Gopalakrishnan, D. Damien and M. M. Shaijumon, *ACS Nano*, 2014, **8**, 5297–5303.
39 H. D. Ha, D. J. Han, J. S. Choi, M. Park and T. S. Seo, *Small*, 2014, **10**, 3858–3862.
40 H. F. Dong, S. S. Tang, Y. S. Hao, H. Z. Yu, W. H. Dai, G. F. Zhao, Y. Cao, H. T. Lu, X. J. Zhang and H. X. Ju, *ACS Appl. Mater. Interfaces*, 2016, **8**, 3107–3114.
41 Y. Li, L. B. Tang, R. J. Li, J. Z. Xiang, K. S. Teng and S. P. Lau, *Chin. Phys. B*, 2019, **28**, 037801.
42 A. Grillo and A. Di Bartolomeo, *Adv. Electron. Mater.*, 2021, **7**, 2000979.
43 C. Y. Wu, Z. Q. Pan, Y. Y. Wang, C. W. Ge, Y. Q. Yu, J. Y. Xu, L. Wang and L. B. Luo, *J. Mater. Chem. C*, 2016, **4**, 10804–10811.
44 Z. Wang, F. H. Liu, Y. J. Gu, Y. G. Hu and W. P. Wu, *J. Mater. Chem. C*, 2022, **10**, 1097–1104.

 This journal is © The Royal Society of Chemistry 2023